Electronic Supplementary Information

Two Dimensional MoS_2 Meets Mn-Porphyrin via Intercalation to Enhance the Electrochcatalytic Activity Toward Hydrogen Evolution

Ik Seon Kwon,[a,†] *In Hye Kwak,*[a,†] *Hafiz Ghulam Abbas,*[b,†] *Hee Won Seo,*[a] *Jaemin Seo,*[a] *Kidong Park,*[a] *Jeunghee Park,*[*,a] *and Hong Seok Kang*[*,c]

[a] Department of Chemistry, Korea University, Jochiwon 339-700, Republic of Korea; E-mail: parkjh@korea.ac.kr

[b] Department of Nanoscience and Nanotechnology, Jeonbuk National University, Chonju, Chonbuk 560-756, Republic of Korea

[c] Department of Nano and Advanced Materials, College of Engineering, Jeonju University, Chonju, Chonbuk 560-759, Republic of Korea; E-mail: hsk@jj.ac.kr

[†] I.S.K., I.H.K., and H.G.A. equally contribute.

Contents

IV. References

I. Experimental

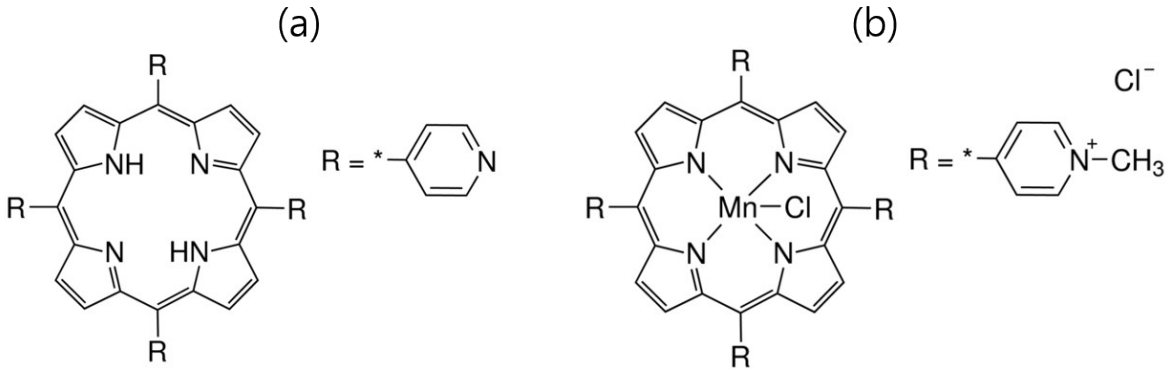

Scheme S1. Structures of (a) 5,10,15,20-tetra(4-pyridyl)-21H,23H-porphine and (b) Mn-5,10,15,20-tetra(4-pyridyl)-21H,23H-porphine chloride tetrakis(methochloride) used as intercalants, which are referred to as H2P and MnP, respectively.

Synthesis. All chemicals were purchased from Aldrich-Sigma Co. MoS_2 nanostructures were synthesized using a hydrothermal method. Ammonium tetrathiomolybdate ($(NH_4)_2MoS_4$, 0.254 mmol, 66 mg) was dissolved in deionized water (20 mL). Then, 0.013 mmol of porphyrin was added: 5,10,15,20-tetra(4-pyridyl)-21*H*,23*H*-porphine (molecular weight (MW) = 618.69 g), manganese (III) 5,10,15,20-tetra(4-pyridyl)-21*H*,23*H*-porphine chloride tetrakis(methochloride) (MW = 909.01 g). The molar ratio of H2P (or MnP) to MoS_2 precursors was adjusted as 5%, due to a limit of solubility. **Scheme S1** shows the structure of the precursors. The reaction mixture was transferred to a Teflon-lined stainless-steel autoclave. A hydrothermal reaction was performed at 180 °C for 12 h in an electric oven. The product was collected by centrifugation, washed thoroughly with deionized water and acetone several times, and then vacuum-dried at room temperature. We also used 0.013 mmol $MnCl_2{\cdot}4H_2O$ (MW = 197.91 g) instead porphyrin and employed the same procedure to synthesized 5% Mn-containing MoS_2 nanosheets.

Characterization. The products were characterized by scanning electron microscopy (SEM, Hitachi S-4700), and field-emission transmission electron microscopy (FE TEM, FEI TECNAI G2 200 kV, Jeol JEM 2100F, HVEM). Energy-dispersive X-ray fluorescence spectroscopy (EDX) with elemental maps was measured using a TEM (FEI Talos F200X) operated at 200 keV that equipped with high-brightness Schottky field emission electron source (X-FEG) and Super-X EDS detector system (Bruker Super-X). This EDX has powerful sensitivity and resolution in the low photon energy region. Fast Fourier-transform (FFT) images were generated by the inversion of the TEM images using Digital Micrograph GMS1.4 software (Gatan Inc.). High-resolution X-ray diffraction (XRD) patterns were obtained using the 9B and 3D beamlines of the Pohang Light Source (PLS) with monochromatic radiation (λ = 1.54595 Å). XRD pattern measurements were also carried out in a Rigaku D/MAX-2500 V/PC using Cu K_α radiation (λ = 1.54056 Å). X-ray photoelectron spectroscopy (XPS) measurements were performed using the 8A1 beam line of the PLS, as well as a laboratory-based spectrometer (Thermo Scientific Theta Probe) using a photon energy of 1486.6 eV (Al Kα).

X-ray absorption near edge spectra (XANES) and extended X-ray absorption fine structure (EXAFS) spectra at the Mo K-edge were collected in transmission mode using the 10C beam line of the PLS with a ring current of 350 mA at 3.0 GeV. Energy calibration was carried out by simultaneously measuring the reference spectrum of Mo metal foil. Least-squares fits of EXAFS data were performed using the Athena and Artemis software packages, version 0.9.25. Electron spin resonance (ESR) measurements were performed on a Bruker EMX-Plus spectrometer at room temperature. The samples (4 mg) were loaded in a quartz tube. The microwave frequency was 9.644564 GHz, and the microwave power was fixed to 20 mW to

avoid saturation. The magnetic properties were measured by means of a superconducting quantum interference device (SQUID, Quantum Design) magnetometer.

Electrochemical Measurements. Experiments were carried in a three-electrode cell connected to an electrochemical analyzer (CompactStat, Ivium Technologies). HER electrocatalysis in 0.5 M H_2SO_4 (or 1.0 M phosphate buffer solution (PBS), 1.0 M KOH electrolyte) was measured using a linear sweeping from 0 to -0.8 V (vs. RHE) with a scan rate of 2 mV s^{-1}. A saturated calomel electrode (SCE, KCl saturated, Basi Model RE-2BP) or Ag/AgCl electrode (saturated with 4M KCl, Pine Co.) was used as reference electrode, and a graphite rod (6 mm dia. × 102 mm long, 99.9995%, Pine Instrument) was used as counter electrode. The electrolyte was purged with H_2 (ultrahigh grade purity) during the measurement. The applied potentials (E) reported in our work were referenced to the reversible hydrogen electrode (RHE) through standard calibration. For example, in 0.5 M H_2SO_4 electrolyte (pH 0), E (vs. RHE) = E (vs. SCE) + E_{SCE} (= 0.241 V) + 0.0592 pH = E (vs. SCE) + 0.241 V. The overpotential (η) was defined as E (vs. RHE). 4 mg sample was mixed with 1 mg carbon black (Vulcan XC-72) dispersed in Nafion (20 μL) and isopropyl alcohol (0.98 mL). The catalyst materials (0.390 mg cm^{-2}) were deposited on a glassy carbon (GC) rotating disk electrode (RDE, area = 0.1641 cm^2, Pine Instrument), and a rotation speed of 1600 rpm was used for the linear sweep voltammetry (LSV) measurements. The Pt/C (20 wt.% Pt in Vulcan carbon black, Aldrich-Sigma) tested as reference sample using the same procedure.

Electrochemical impedance spectroscopy (EIS) measurements were carried out for the electrode in an electrolyte by applying an AC voltage of 10 mV in the frequency range of 100 kHz to 0.1 Hz at a bias voltage of -0.15 V (vs. RHE). To measure double-layer capacitance

via CV, a potential range in which no apparent Faradaic processes occur was determined from static CV. This range is 0.1–0.2 V. All measured current in this non-Faradaic potential region is assumed to be due to double-layer capacitance. The charging current, i_c, is then measured from CVs at multiple scan rates. The working electrode was held at each potential vertex for 10 s before beginning the next sweep. The double-layer capacitance current density (J) is equal to the product of the scan rate (ν) and the electrochemical double-layer capacitance (C_{dl}), as given by equation $J = \nu C_{dl}$, Thus, a plot of J as a function of ν yields a straight line with a slope equal to C_{dl}. The scan rates were 20–100 mV s^{-1}.

TOF Calculation. The active site density and per-site turnover frequency (TOF) have been estimated as follows. It should be emphasized that since the nature of the active sites of the catalyst is not clearly understood yet and the real surface area for the nanostructured heterogeneous catalyst is hard to accurately determine, the following result is really just an estimation.

To estimate the active surface site density, we used the C_{dl} value, and further calculate the electrochemically active surface area. The roughness factor (basically the surface area ratio between the catalyst vs. the metal electrodes (0.035 mF cm^{-2}),[S1] for example, is 43.0 mF cm^{-2}/0.035 mF cm^{-2} = 1229 for MnP-MoS_2.

The number of catalytic sites on the surface of flat catalyst can be calculated based on the crystal structure of distorted octahedral-phase 1T' MoS_2. Using the lattice parameters of 1T' phase MoS_2 (we calculated as a = 3.27 Å, b = 3.17 Å, γ = 119°) and assuming one active site per MoS_2 (which translates into on reactive sites per unit cell), the density of surface active sites is: $1/(0.5 \times 3.17 \times 3.27 \times \sin 119°) \times 10^{16}$ cm^{-2} = 2.2×10^{15} atom cm^{-2}).[S2] Our DFT

calculation shows that the basal S sites above the center site (H or Mn) of porphyrin (5%) are most active sites, so the number of surface active sites is calculated as $0.05 \times 2.2 \times 10^{15}$ atom $cm^{-2} = 1.1 \times 10^{14}$ atom cm^{-2}. The density of surface active sites (m) of H2P-MoS_2 and MnP-MoS_2 on geometric area: 1.1×10^{14} atom $cm^{-2} \times 1229$ (= roughness factor) $= 1.35 \times 10^{17}$ atom cm^{-2}.

The total number of hydrogen (H_2) gas turns overs was calculated from the current density (J in mA cm^{-2}) according to n_{H2} = J (mA cm^{-2})/1000 mA × 1 C s^{-1} × 1 mol e^-/96486 C × (1 mol H_2/2 mol e^{-1}) × (6.022×10^{23} H_2 molecules/1 mol H_2) = 3.12×10^{15} H_2 s^{-1} cm^{-2} per mA cm^{-2}.

For MnP-MoS_2, the per-site TOF at $\eta = 0.18$ V (with a current density of 187 mA cm^{-2}) is n_{H2}/m (= density of surface active sites) $= 187 \times 3.12 \times 10^{15}$ H_2 s^{-1} cm^{-2} / 2.7×10^{17} atom cm^{-2} = 2.1 H_2 s^{-1}. In the case of H2P-MoS_2, the TOF was estimated as 1.2 s^{-1}, respectively, at 0.18 V.

We summarized the TOF values at 0.18 V as follows.

Guest	J (mA cm^{-2}) at 0.18 V	n_{H2}	Roughness factor	m	TOF
H2P	25.5	8.0×10^{16}	903	9.93×10^{16}	0.81
MnP	187	5.8×10^{17}	1229	1.35×10^{17}	4.3

Computations. Geometry optimizations were performed using the Vienna ab-initio simulation package (VASP).[S3] The electron-ion interactions were described using the projector-augmented wave (PAW) method.[S4] Attractive van der Waals interactions were included using Grimme's correction for the Perdew–Burke-Ernzerhof (PBE)-D3 method.[S5]

For structural optimization, the atoms were relaxed in the direction of the Hellmann-Feynman force using the conjugate gradient method with an energy cut-off of 520 eV, until a stringent convergence criterion of 1 meV/Å was satisfied. Lattice constants were optimized using the PBE-D3 exchange-correlation functional. The *k*-point sampling was performed using Γ-centered 6×6×4 points, which gave the total energy of the (4×4) MoS_2 complex in the 1T' phase within 1 meV. For systems including Mn ions, we applied the PBE+U method to treat on-site screened Coulomb interaction.[S6] For the Hubbard parameter U_{eff} = U-J, we used a value of 3.20 eV.

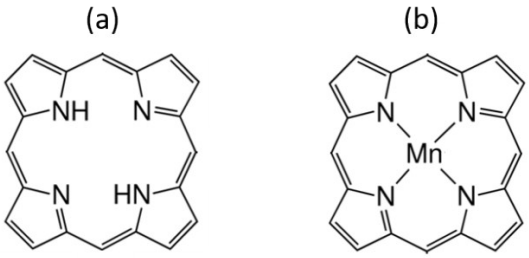

Scheme S2. Structures of (a) 21H,23H-porphine and (b) Mn(II or III)-21H,23H-porphine used as intercalants for calculation , which we referred to as H2-PPY and Mn-PPY, respectively. In the case of Mn(III)-21H,23H-porphine, OH is coordinated to compensate the positive charge of Mn ion.

We used 21H,23H-porphine and Mn(II or III)-21H,23H-porphine as intercalants (**Scheme S2**). The weak crystal field splitting is not consistent with our PBE calculation for Mn-PPY, which predicted an incorrect magnetic moment of $3\mu_B$. However, this discrepancy could be resolved when the PBE+U method is employed with U_{eff} = 3.20 eV. Referring to the high spin states of the Mn-PPY molecule, we expect that their MoS_2 complex may also exhibit nonzero magnetic moment. In our calculation, this was indeed borne out by the calculated

magnetic moment (μ= 3.99 μ_B) of the complex ((4×4) MoS_2-Mn-PPY), which included one MnP molecule in the (4×4) MoS_2 layer. At room temperature, paramagnetic systems should display a net magnetic moment of zero due to thermal randomization. Therefore, to calculate electronic structure at room temperature, it is inappropriate to model all occupied states of Mn-PPY as spin-paired. In the first-order approximation, the randomization can be described effectively if (1) we adopt a supercell twice as large as that for (4×4) MoS_2-MnP along the *c* direction, i.e., (4×4) $2MoS_2$-2(Mn-PPY) containing two Mn-PPY molecules between two pairs of MoS_2 layers, and (2) spins due to two Mn-PPY molecules are forcefully cancelled out in antiferromagnetic coupling. A calculation based on the supercell of (4×4) MoS_2-Mn-PPY should be incorrect, because it amounts to assuming that spins of adjacent cells couple ferromagnetically.

The adsorption energies and activation barriers for an H^+ ion at different adsorption sites were calculated using the climbing image-nudged elastic band (CINEB) method.[S7] For simplicity, we employed a slab geometry in which a supercell included two MoS_2 layers and one porphyrin molecule. The coordinate system is defined so that the MoS_2 layer lies on the *ab* plane parallel to the XY plane. Two lowest sublayers (i.e., all Mo ions as well as one-half of S atoms on the lower MoS_2 layer) were fixed, while all other atoms were permitted to relax freely. For computational efficiency, we adopted a supercell of (4×4) $2MoS_2$ with one PPY molecule. Again, the CINEB calculation was done with spin-polarization for the Mn-PPY complex. More accurate calculation should require antiferromagnetic coupling of spins in a supercell twice as large. The error in our simpler calculation can be roughly estimated from $\Delta E_{AFM\text{-}FM}$, the difference in total energy for the complex along the *c* axis with the antiferromagnetic and ferromagnetic couplings. The value of $\Delta E_{AFM\text{-}FM}$ (=16 meV) per PPY

molecule is indeed small, supporting the accuracy of our calculation.

II. Supporting Tables

Table S1. Fitting parameters of EXAFS data for the MoS_2 samples (see **Fig. 2b**). The FT curves of EXAFS were fitted to two scattering shells. A least-squares curve parameter method was performed using the ARTEMIS module of IFEFFIT and USTCXAFS software packages.

Sample	Scattering Path	R (Å)[a]	CN[b]	ΔE (eV)[c]	σ^2 (Å^2)[d]
MoS_2	Mo-S	2.40	6.2 ± 0.3	1.3	0.0028
	Mo-Mo	3.16	4.2 ± 0.8	0.8	0.0036
H2P-MoS_2	Mo-S	2.41	5.8 ± 0.9	-1.4	0.0080
	Mo-Mo	2.76	1.1 ± 0.7	-2.0	0.0072
MnP-MoS_2	Mo-S	2.40	5.0 ± 0.6	-3.4	0.0078
	Mo-Mo	2.78	1.0 ± 0.5	4.9	0.0045

[a] Distance between scattering atoms. The FT curve of the 2H phase MoS_2 are characterized by two main peaks at 2.40 and 3.16 Å, corresponding to the nearest Mo–S and Mo–Mo bonds, respectively.[S8,S9] In contrast, in the FT curves of H2P-MoS_2 and MnP-MoS_2, the second peak (related to the nearest Mo–Mo bond) shows a noticeable shift from 3.16 to 2.76-2.78 Å.

[b] Coordination number of Mo atoms. The intensity of this peak is nearly reduced by 1/3, corresponding to the coordination number of Mo-Mo decreased significantly. All these results indicate that the intercalated MoS_2 adopts a distorted octahedral coordination.

[c] Edge energy shift, representing between the energy grids of experimental and theoretical data. [d] Debye-Waller factor, which measures the static and thermal disorder, is larger for H2P-MoS_2, and MnP-MoS_2 than MoS_2. It suggests that the intercalation produces a broad range of Mo-S and Mo-Mo distances.

Table S2. The $\eta_{J=10}$ value and Tafel slope (*b*) for the LSV curves measured in pH 0, 7.4, and

Sample	pH 0 (0.5 M H_2SO_4)		pH 7.4 (1.0 M PBS)		pH 14 (1.0 M KOH)	
	$\eta_{J=10}$ (mV)	*b* (mV dec^{-1})	$\eta_{J=10}$ (mV)	*b* (mV dec^{-1})	$\eta_{J=10}$ (mV)	*b* (mV dec^{-1})
Pt/C	27	30	20	30	60	30
MoS_2	202	54	350	83	435	89
H2P-MoS_2	160	44	263	73	293	78
MnP-MoS_2	125	35	210	68	250	68

14 (see the data Figure S6).

Table S3. Impedance parameters for the equivalent circuit that was shown in **Figure S7**, and the double-layer capacitance (C_{dl}) as shown in **Figure S8**.

`	EIS		C_{dl} (mF cm^{-2})
Samples	R_s (Ω)	R_{ct} (Ω)	
MoS_2	5.0	71.5	16.5
H2P-MoS_2	4.7	20.0	31.6
MnP-MoS_2	4.0	9.2	43.0

Table S4. Comparison of HER performance (in pH 0) of MoS_2 in the literatures.

Reference	**Materials**	**Phase**	**$E_{J=10}$ (mV) at 10 mA cm^{-2}**	**Tafel slope (mV dec^{-1})**
S10	MoS_2	2H	~190	50
S11	1T MoS_2	1T	200	40
S12	Ammoniated MoS_2	2H	320	45
S13	MoS_2 single-layer nanosheets	2H	N/A	50
S14	MoS_2 nanosheet	1T	175	41
S2	1T MoS_2	1T	154	43
S15	1T' MoS_2 monolayer	1T'	300	61
S16	1T/2H MoS_2	1T/2H	234	46
S17	Functionalized MoS_2 nanosheet	1T	348	75
S18	1T MoSSe nanodots	1T	140	40
S8	DMPD intercalatedMoS_2	1T'	160	38
Present work	MnP-intercalated MoS_2	1T'	125	35

N/A: Not applicable

Table S5. Comparison of H_2 evolution turnover frequency (TOF) of MoS_2 (in pH 0) in the literatures.

Reference	Materials	Phase	TOF (H_2 s^{-1})
S2	Porous 1T MoS2	1T	0.5 at 0.153 V
S10	Defect-rich MoS_2	2H	0.725 at 0.3 V
S13	Single layer MoS_2	2H	0.019-0.046 at 0 V
S19	S depleted MoS_2	2H	8.74 at 0.2 V
S15	1T' monolayer MoS_2	1T′	3.8±1.6 at 0.077 V
S16	1T/2H MoS_2	1T/2H	~ 0.15 at 0.2 V
S20	Vacancy rich surface MoS_2	2H	~9 at 0.2 V
S21	Zn-doped MoS_2	2H	~ 5 at 0.2 V
S22	Pd-MoS_2	2H	16.54 at 0.2 V
Present work	MnP-intercalated MoS_2	1T′	4.3 at 0.18 V

III. Supporting Figures

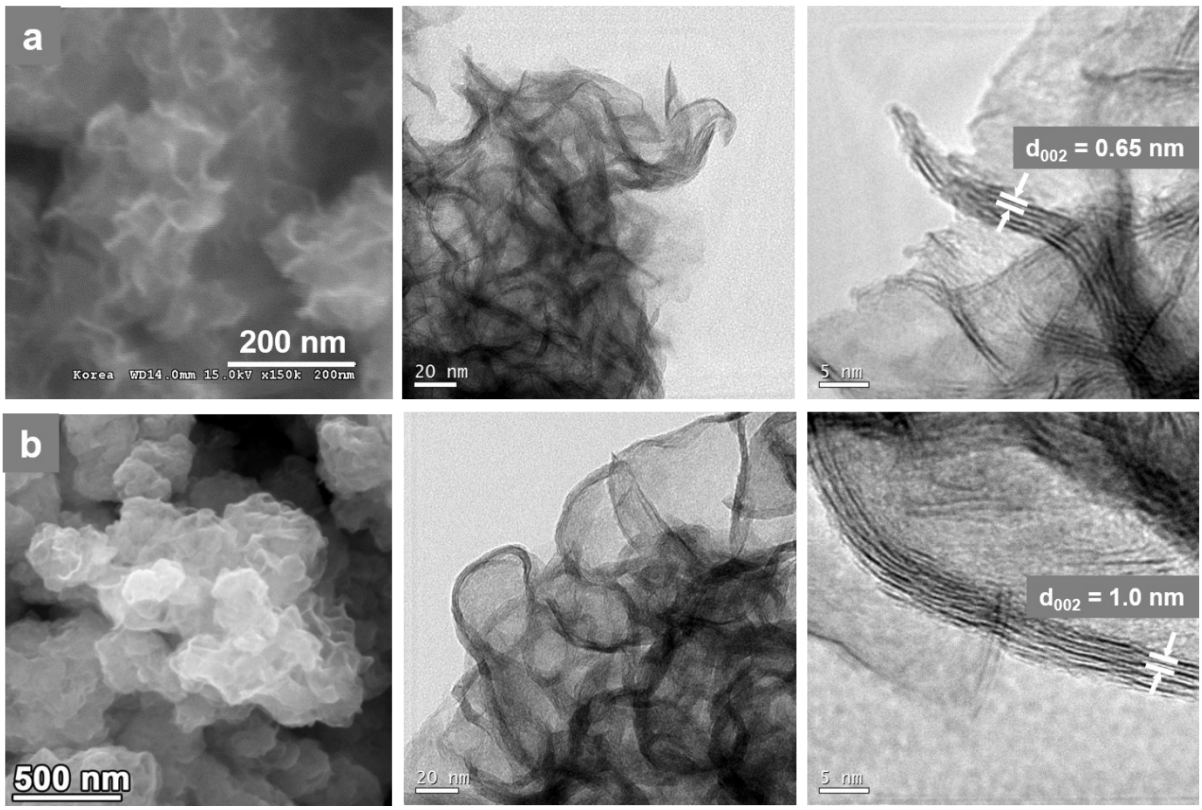

Figure S1. SEM and TEM images of (a) MoS_2 and (b) H2P-MoS_2. The MoS_2 and H2P-MoS_2 consisted of the flower-like MoS_2 nanosheets that assembled into the nanoparticles with the size of 100–300 nm. The thickness of the layers was 5-7 nm. The lattice-resolved TEM image shows that the average distance between adjacent MoS_2 layers (d_{002}) is 6.5 and 10 Å, for MoS_2 and H2P-MoS_2, respectively.

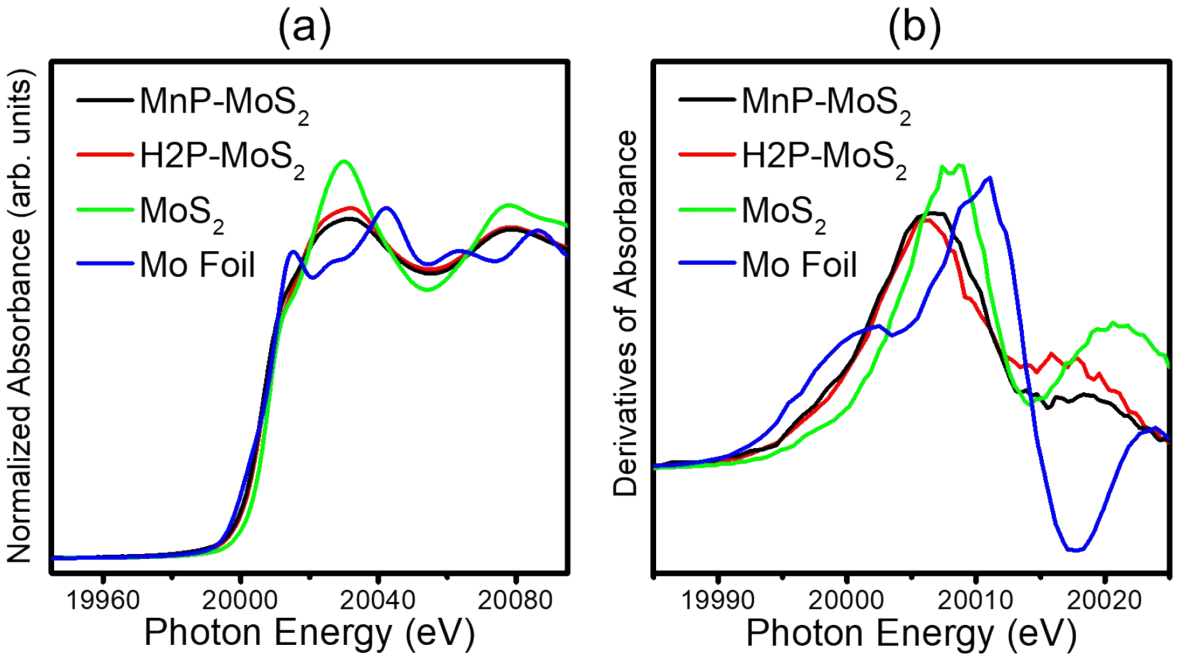

Figure S2. (a) XANES spectra at the Mo K edge for Mo (foil), MoS_2, H2P-MoS_2, and MnP-MoS_2. (b) First derivative of absorbance curve in the onset region.

The evolution of the local crystal structure of MoS_2 upon the intercalation was probed with Mo K-edge X-ray absorption near edge spectra (XANES) analysis. In the Fourier transform (FT) profiles (in real space) of the extended X-ray absorption fine structure (EXAFS), the peaks indicate the distances to nearest neighbor atoms. The profiles of the H2P-MoS_2 and MnP-MoS_2 are significantly different from that of MoS_2, suggesting a remarkable change in the local atomic arrangements. The absorption edge shows a red shift following the order Mo foil > H2P-MoS_2 and MnP-MoS_2 > MoS_2. The first derivative of absorption curve in the onset region shows a peak at 20000 and 20008 eV, respectively, for Mo foil and 2H phase MoS_2. The H2P-MoS_2 and MnP-MoS_2 shows a peak at 20006 eV, indicating the more metallic nature compared to the 2H phase MoS_2.

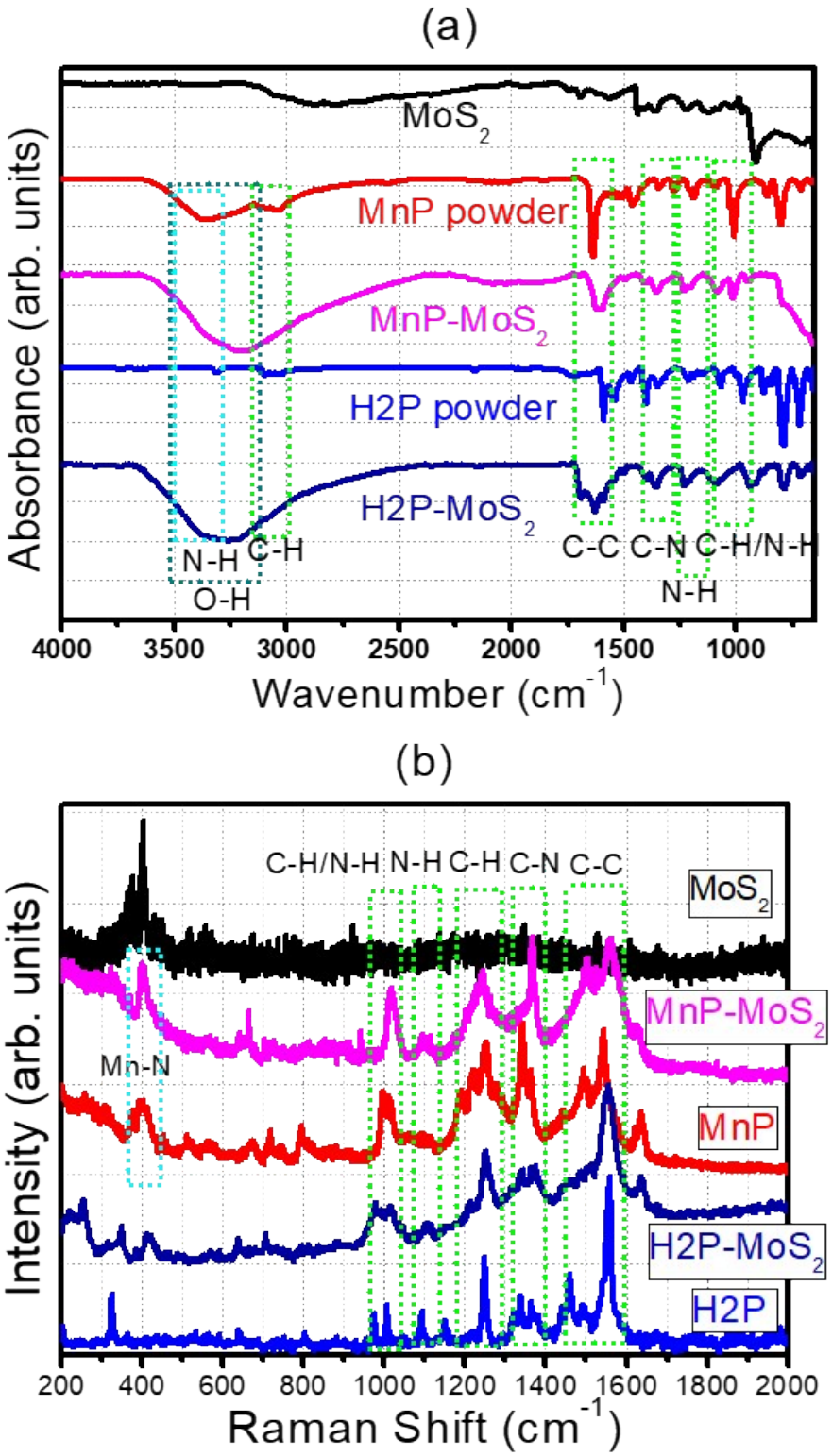

Figure S3. (a) IR and (b) Raman spectra of MoS_2, H2P precursor powder (5,10,15,20-tetra(4-pyridyl)-21H,23H-porphine), H2P-MoS_2, MnP precursor powder (manganese (III)

5,10,15,20-tetra(4-pyridyl)-21*H*,23*H*-porphine chloride tetrakis(methochloride)), and MnP-MoS_2. The peaks of porphyrin ring (C-C, C-N, C-H, and N-H) exist in the MoS_2 complexes.[S23] IR spectrum shows that the strong O-H peaks, indicating the hydrate form of porphyrin. The Raman spectrum of MnP and MnP-MoS_2 exhibits the Mn-N peaks at 400 cm^{-1}.[S24] The MoS_2 exhibit two characteristic Raman peaks of the 2H phase at 380 and 403 cm^{-1}, corresponding to the in-plane E^1_{2g} and out-of-plane A_{1g} vibration modes, respectively. They are overlapped with those of Mn-N at 400 cm^{-1} of MnP. The Raman peaks of 1T' phase: the J_1 peak at 148 cm^{-1}, the J_2 peak at 236 cm^{-1}, and the J_3 peak at 336 cm^{-1}, which are not clearly identified due to the background peaks of porphyrin.[S25]

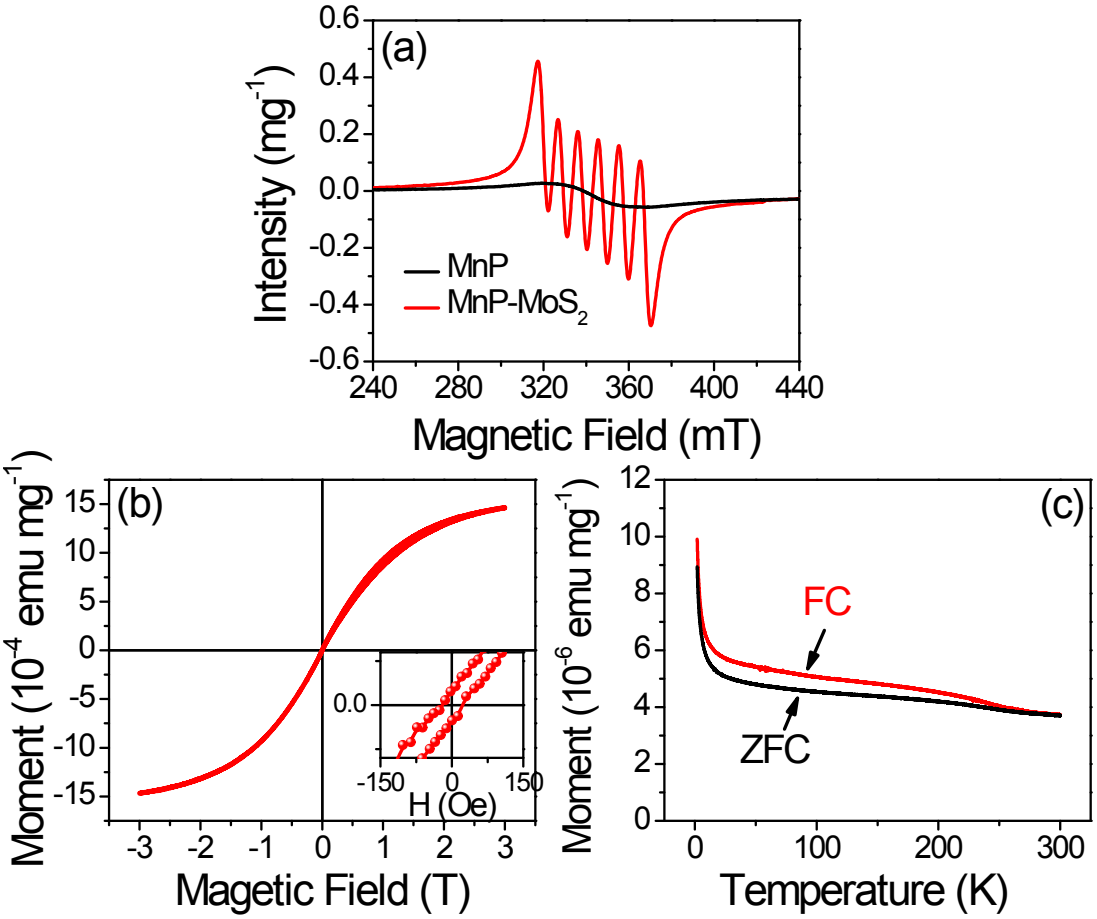

Figure S4. (a) ESR spectra for MnP precursor and MnP-MoS_2; (b) M-H (at 2K) , and (c) M-T curves for MnP-MoS_2.

Electron spin resonance (ESR) measurements were performed for MnP and intercalated MnP-MoS_2 at room temperature. The MnP precursor exhibit no signal, but MnP-MoS_2 shows a sextet signal centered at 344 mT (g = 2.00). The signal can be originated from a high spin d^5 of Mn^{2+} state in MnP molecules.

The magnetic properties of MnP-MoS_2 were measured by the SQUID magnetometer. The magnetization (M) versus magnetic field (H) curves at 2 K. The hysteresis curve in the vicinity of H = 0 suggest their ferromagnetic behavior. The field-cooled (M_{FC}) and zero-field-cooled M (M_{ZFC}) versus T curves with H = 20 Oe, as a function of temperature (2-300 K). The non-zero difference between M_{FC} and M_{ZFC}, owing to the presence of hysteresis, indicates that the ferromagnetism persists to approximately 280 K.

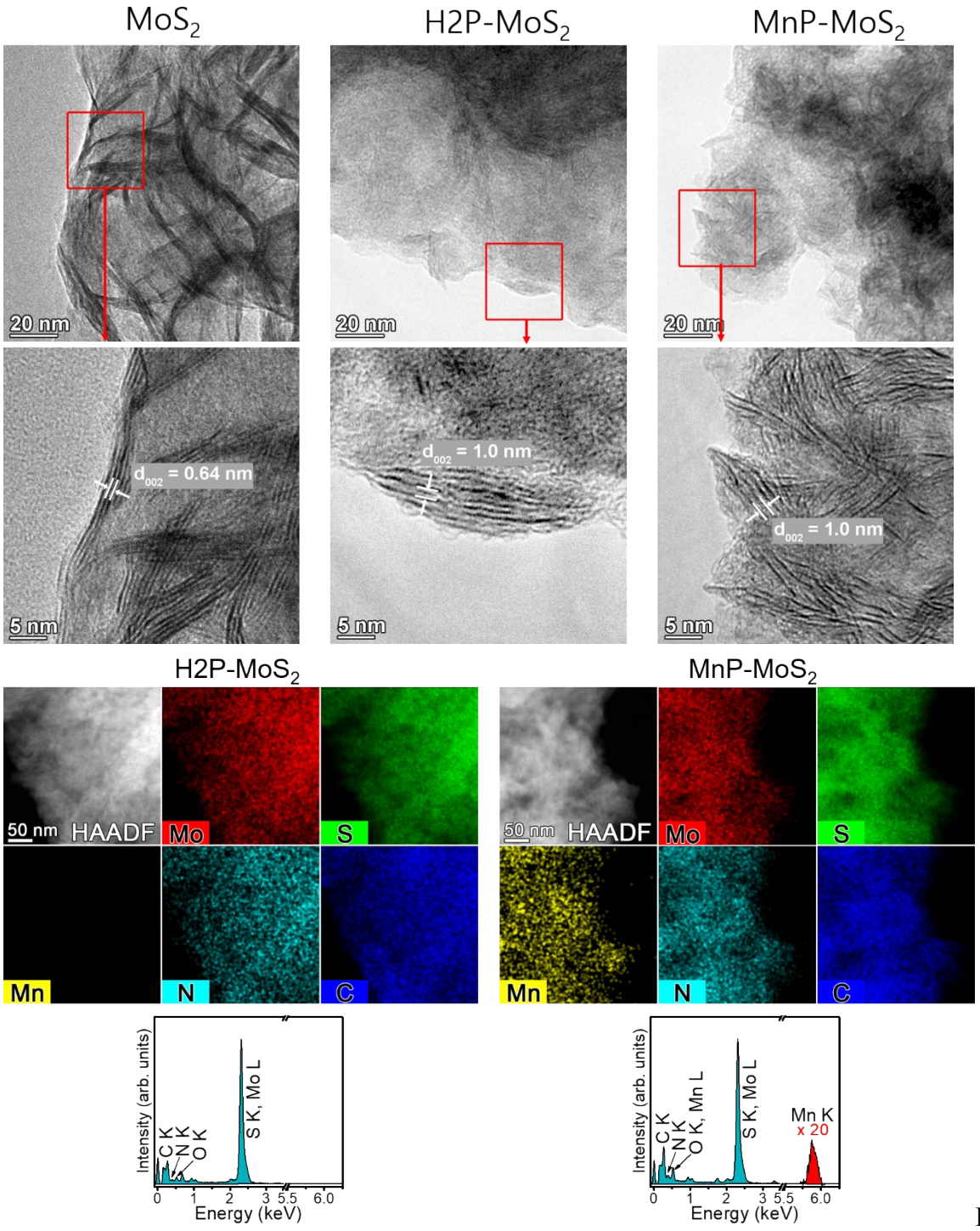

Figure S5. TEM images and EDX data of MoS_2, H2P-MoS_2, and MnP-MoS_2 after 10h chronoamperometric measurement.

The size of nanosheets is 50-100 nm, which is smaller than that of the samples before HER (100-300 nm). The lattice-resolved TEM image shows that the average distance between

adjacent MoS_2 layers (d_{002}) is the same as that of the before samples; 6.5, 10, and 10 Å, respectively, for MoS_2, H2P-MoS_2, and MnP-MoS_2. The EDX mapping and spectrum show that the atoms distribute homogeneously over the entire samples. For MnP-MoS_2, the at% of Mn is about 5%, which remain the same after the HER.

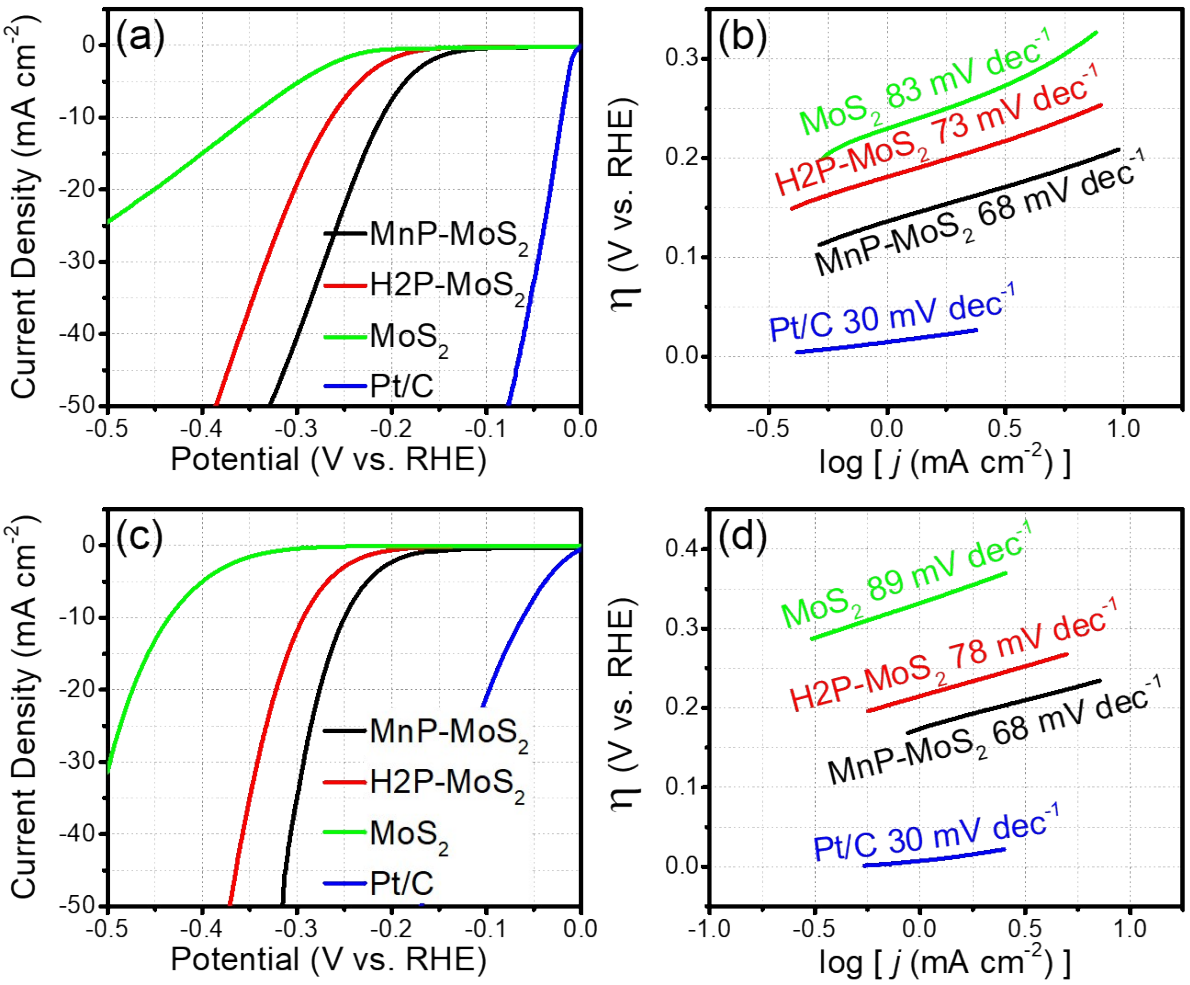

Figure S6. LSV curves (scan rate: 2 mV s^{-1}) for Pt/C, MoS_2, H2P-MoS_2, and MnP-MoS_2 toward HER in H_2-saturated (a) 1 M phosphate buffer solution (pH 7.4) and (c) 1.0 M KOH (pH 14) Corresponding Tafel plots in (b) pH 7 and (d) pH 14, derived from the LSV curves, where the Tafel slope (mV dec^{-1}) is indicated in parentheses. In pH 7.4, the overpotentials required to deliver a current density of 10 mA cm^{-2} ($\eta_{J=10}$) were 0.020, 0.350, 0.263, and 0.210 V for Pt/C, MoS_2, H2P-MoS_2, and MnP-MoS_2, respectively. In pH 14, the respective $\eta_{J=10}$ were 0.060, 0.435, 0.293, and 0.250 V for Pt/C, MoS_2, H2P-MoS_2, and MnP-MoS_2. The data is summarized in Table S2.

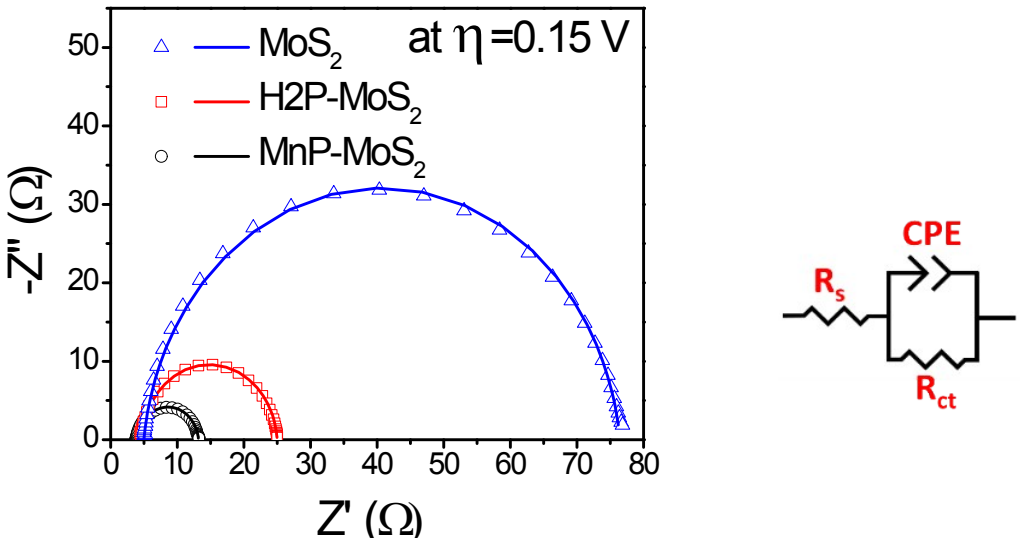

Figure S7. Nyquist plots for EIS measurements from 100 kHz to 0.1 Hz at a representative potential of -0.15 V (vs. RHE) and the equivalent circuit diagram.

Electrochemical impedance spectroscopy (EIS) measurements were performed in the frequency range of 100 kHz–0.1 Hz and an amplitude of 10 mV at η = 0.15 V. In the high-frequency limit and under non-Faradaic conditions, the electrochemical system is approximated by the modified Randles circuit shown on the right of Fig. S5, where R_s denotes the solution resistance, CPE is a constant-phase element related to the double-layer capacitance, and R_{ct} is the charge-transfer resistance from any residual Faradaic processes. A semicircle in the low-frequency region of the Nyquist plots represents the charge transfer process, with the diameter of the semicircle reflecting the charge-transfer resistance. The real (Z') and negative imaginary ($-Z''$) components of the impedance are plotted on the x and y axes, respectively. Simulating the EIS spectra using an equivalent circuit model allowed us to determine R_{ct}, which is a key parameter for characterizing the catalyst-electrolyte charge transfer process. The fitting parameters are listed in Table S2.

The obtained R_{ct} values are 71.5, 20.0, and 9.2 Ω for MoS_2, H2P-MoS_2, and MnP-MoS_2, respectively. The porphyrin intercalated samples have much smaller charge transfer resistance (R_{ct}) than MoS_2. The order of R_{ct} is consistent with that of the HER performance. The reduced charge-transfer resistance plays a major role in enhancing the HER catalytic activity of the intercalated samples.

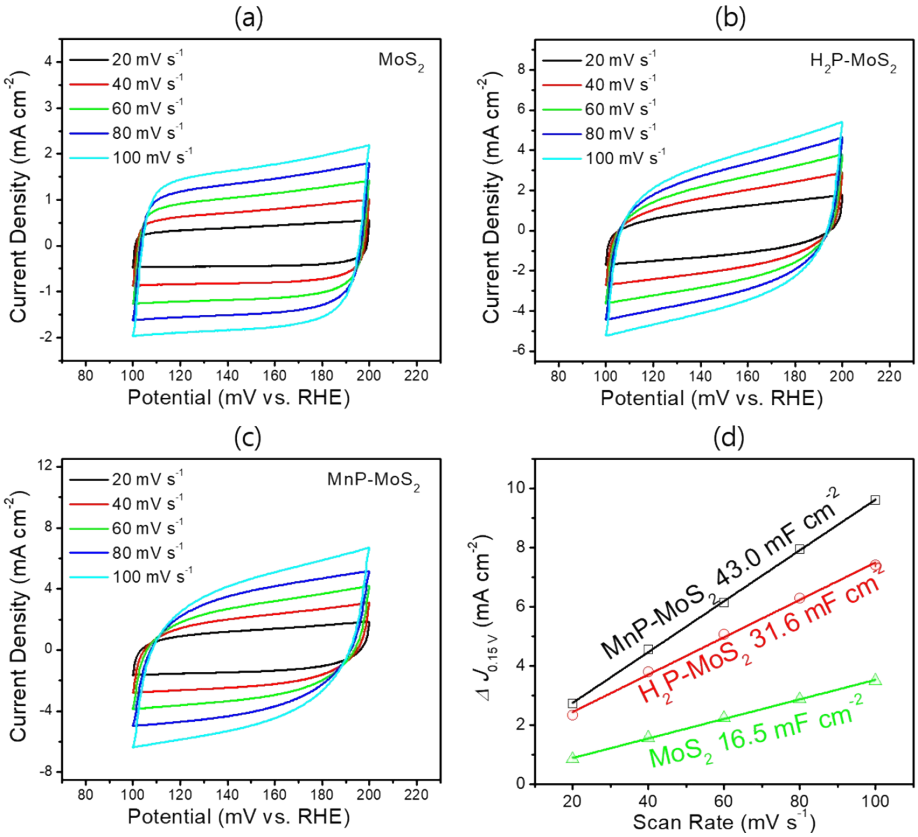

Figure S8. Cyclic voltammograms of (a) MoS_2, (b) H2P-MoS_2 and (c) MnP-MoS_2 in a non-Faradaic region (0.1-0.2 V vs. RHE), at 20–100 mV s^{-1} scan rates and in 0.5 M H_2SO_4 solution. (d) Difference (ΔJ) between the anodic charging and cathodic discharging currents measured at 0.15 V (vs. RHE) and plotted as a function of the scan rate. The value in parenthesis represents the C_{dl}, obtained by the half of the linear slope.

Cyclic voltammograms were measured at 0.1-0.2 V, in a non-Faradaic region, using various scan rates. The double-layer capacitance (C_{dl}) was obtained as the slope (half value) of a linear fit of ΔJ vs. scan rate (20–100 mV s^{-1}), where ΔJ is the difference between the anodic charging (positive value) and cathodic discharging currents (positive value). The C_{dl} values of MoS_2, H2P-MoS_2, and MnP-MoS_2 are 16.5, 31.6, and 43.0 mF cm^{-2}, respectively (see the summary in Table S2), showing a significant increase upon intercalation. The intercalated MoS_2 samples have very rough surfaces and can thus expose a large number of active sites. Therefore, the increased double-layer capacitance leads to the enhanced HER catalytic activity of the intercalated samples. The C_{dl} values follow the same order as that of HER performance: MnP-MoS_2 > H2P-MoS_2 > MoS_2.

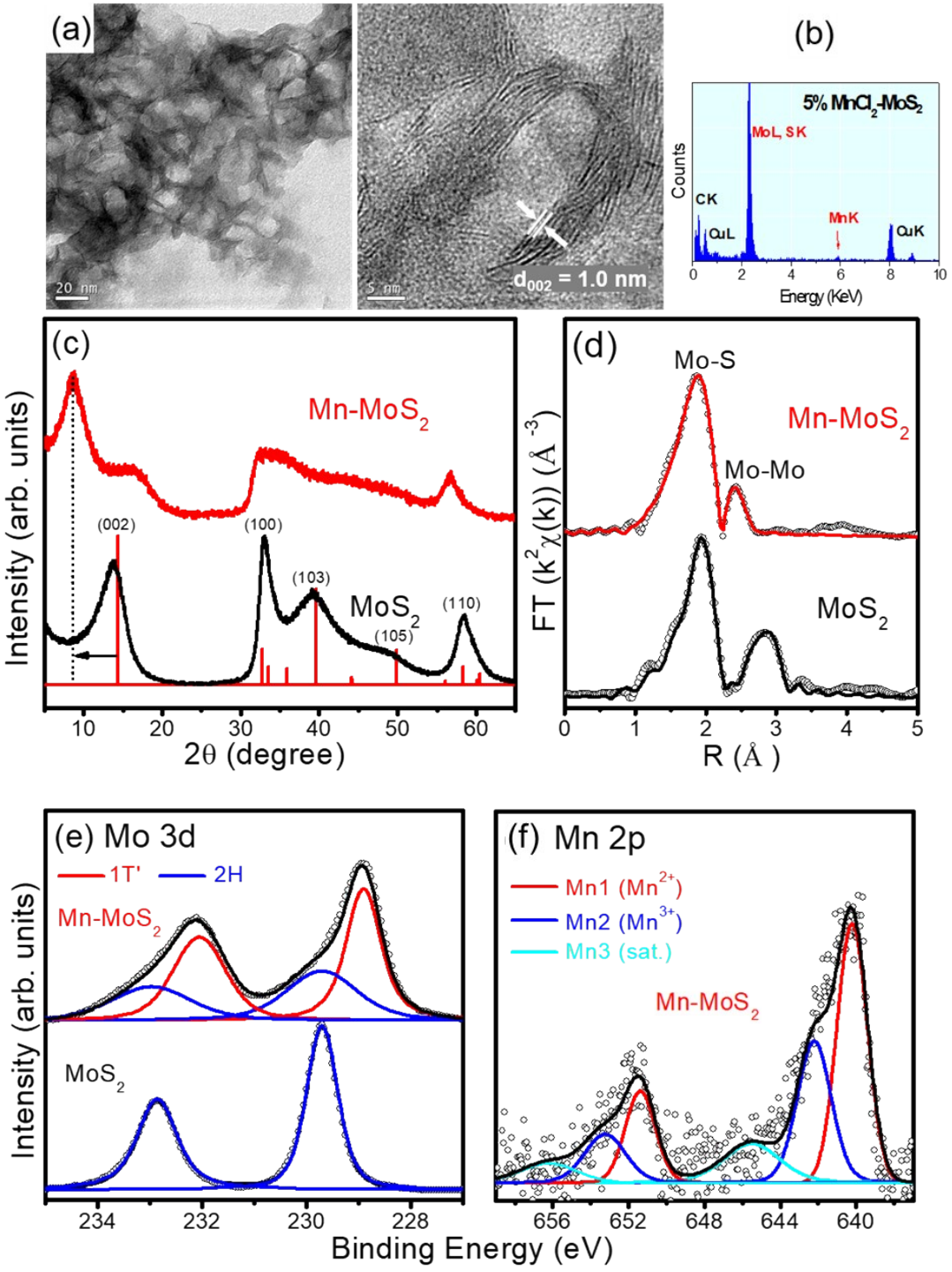

Figure S9. (a) SEM and HRTEM images showing the general morphology of Mn-containing MoS_2. (b) EDX spectrum shows Mn/MoS_2 = 5%. (c) XRD patterns of 2H-MoS_2 and MnP-MoS_2. The peaks were referenced to those of 2H phase shown at the bottom. The (002) peak is shifted to 9°, corresponding to c = 20 Å. (d) Non-phase-corrected k^2 weighted FT EXAFS

data (open circles) at the Mo K edge and their fitting curves (line). The FT curves were fitted to $d_{Mo\text{-}S}$ = 2.40 Å and $d_{Mo\text{-}Mo}$ = 2.78 Å, corresponding to the values of 1T′ phase. (e) Fine-scan XPS data of Mo 3*d* peaks. The data (open circles) are fitted by a Voigt function, and the sum of the resolved bands is represented by the black line. The peak was resolved into two bands: 1T' phase (red) at 228.9 and 2H phase (blue) at 229.7 eV. The fraction of the 1T′ phase band was determined as 60%, confirming that this is the major phase. (f) Fine-scan XPS data of Mn $2p_{3/2}$ and $2p_{1/2}$ peaks. The peak of Mn $2p_{3/2}$ was resolved into three bands: Mn1 (Mn^{2+}, red) at 640.2 eV, Mn2 (Mn^{3+}, blue) at 642.2 eV, and Mn3 (satellite of Mn^{2+}, turquoise) at 645 eV. The ratio of Mn^{2+}:Mn^{3} is 6:4. The paramagnetic Mn^{2+} ions produce the satellite peak at 645 eV.

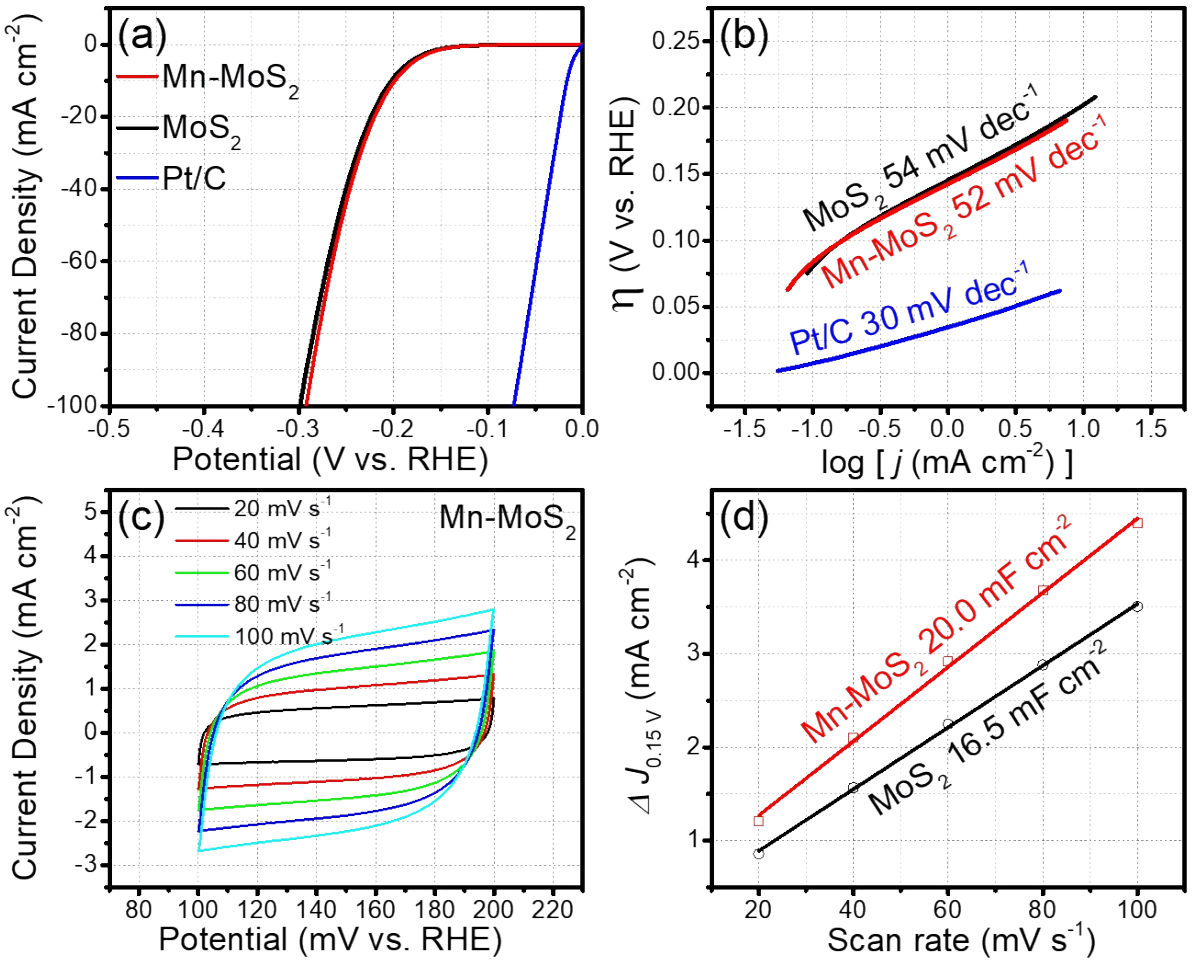

Figure S10. (a) HER LSV curves (scan rate: 2 mV s^{-1}) for Mn-containing MoS_2 samples (as shown in Figure S7), with Pt/C and 2H-MoS_2 in H_2-saturated 0.5 M H_2SO_4. The overpotential for a current density of 10 mA cm^{-2} ($\eta_{J=10}$) is 0.197 V, which is close to 0.205 V of 2H-MoS_2. (b) Tafel plot derived from the LSV curve, where the Tafel slope is indicated in parentheses. The Tafel slope is 52 mV dec^{-1}, which is close to 54 mV dec^{-1} of 2H-MoS_2. (c) CV in a non-Faradaic region (0.1-0.2 V vs. RHE) at 20–100 mV s^{-1} scan rates. (d) Difference ($\Delta J_{0.15}$) between the anodic charging and cathodic discharging currents measured at 0.15 V (vs. RHE) and plotted as a function of the scan rate. The value in parenthesis represents the C_{dl}, obtained by the half of the linear slope. The C_{dl} value is 20.0, mF cm^{-2}, which is slightly larger than that of 2H-MoS_2 (16.5 mF cm^{-2}).

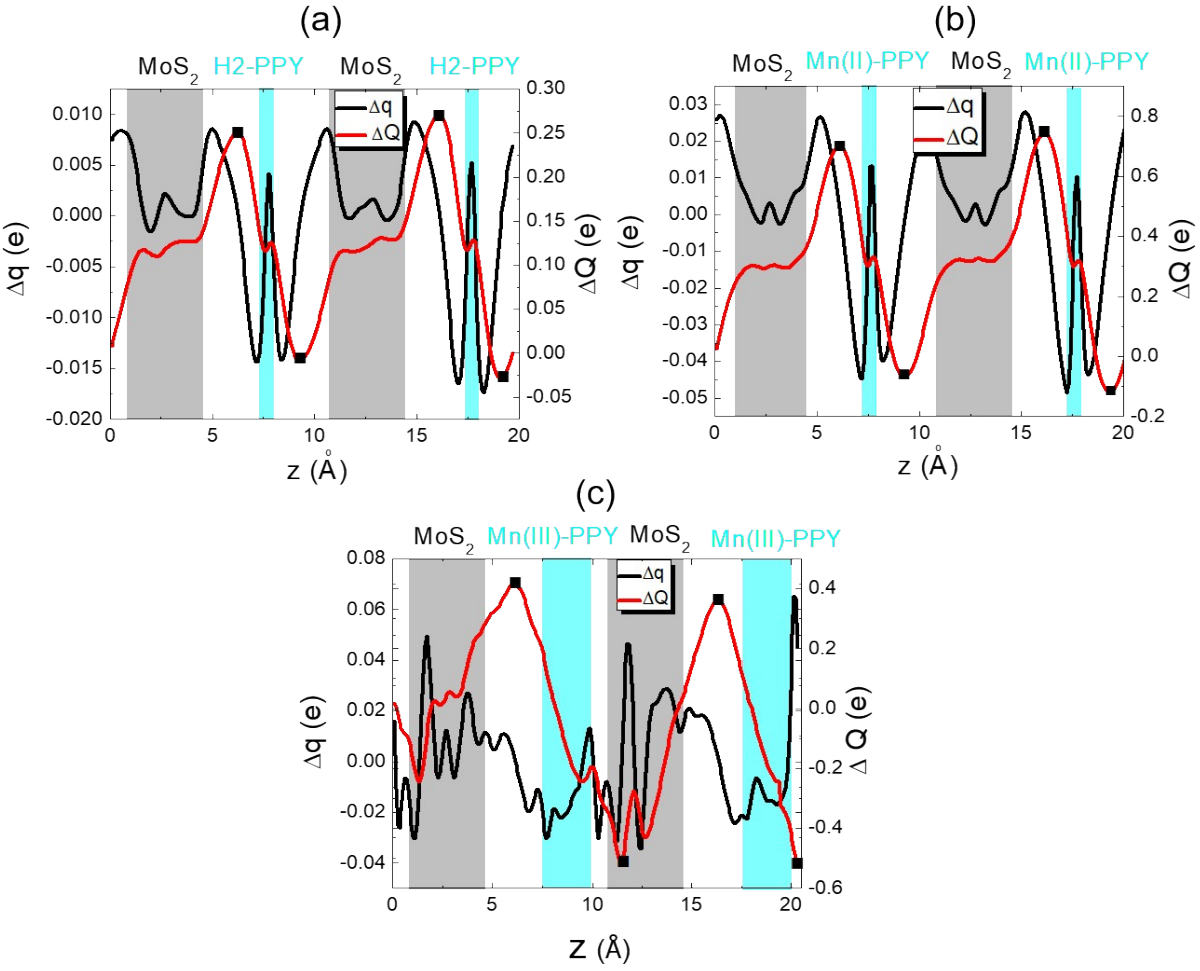

Figure S11. Δq and ΔQ of (a) (4×4) 2MoS_2-2(H2-PPY), (b) (4×4) 2MoS_2-2(Mn(II)-PPY) and (c) (4×4) 2MoS_2-2(Mn(III)-PPY) versus z: z_{min} and z_{max} values corresponding to $Q_{min}(z)$ and $Q_{max}(z)$ are shown by filled squares (■), respectively.

Following our previous studies, the amount of the charge transfer was calculated.[S16, S17] The change in electron density (expressed in *e* Å^{-3}) along the *c* (= *z*) axis generated by the intercalation process was defined as $\Delta\rho = \rho(z)\{MoS_2\text{-PPY}\} - \rho(z)\{MoS_2\} - \rho(z)\{PPY\}$, averaged over the *xy* plane in a supercell. The total electron density change (*e*) was defined as $\Delta q(z) = \Delta\rho(z)\Delta V$, where ΔV is the volume of a fine grid, *i.e.*, $\Delta V = V_{cell}/N_c$, in which V_{cell} is the total volume of the supercell and N_c is the number of fine grids. The thickness of each MoS_2 layer was defined on the basis of the *z* coordinates of the S atoms in the upper and lower sublayers (S_L and S_U), with $z(S_L) < z(S_U)$. The thickness of PPY molecules was obtained from the minimum and maximum *z* coordinates of its atoms. The actual thickness

might be larger than that obtained using this definition, if the finite atomic size is taken into account. In addition, $Q(z)$, displayed on the right vertical axis represents the accumulated excess charge in the interval [0, z]: $Q(z)=\sum_{0}^{z'<z}\Delta q(z')$, i.e., the integration of charge difference $\Delta q(z')$ within $z' < z < c$. The amount of charge transfer was defined as $\Delta Q = Q_{max} - Q_{min}$, where Q_{max} and Q_{min} correspond to the maximum and minimum charge values in the regions (marked by ■) adjacent to the MoS_2 layers and porphyrin molecules, respectively. The calculated ΔQ value was 0.85e and 0.89e for Mn(II)-PPY and Mn(III)-PPY, respectively, which is larger than that (0.27e) of the H2-PPY. The larger ΔQ value confirmed that a more significant charge transfer took place.

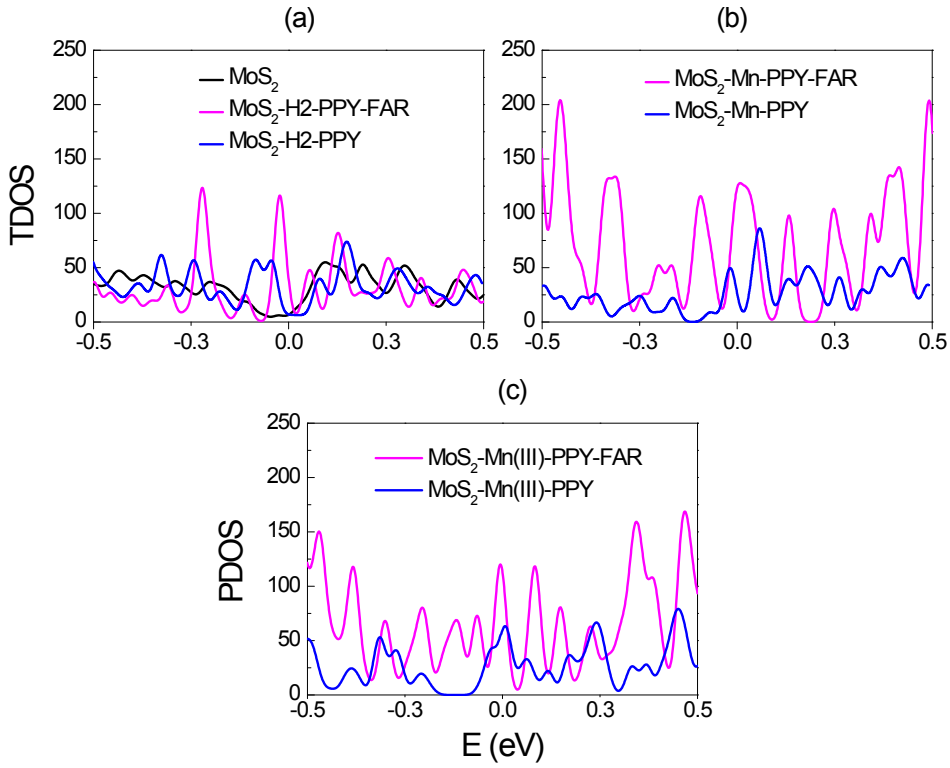

Figure S12. TDOS of 1T' phase (a) (4×4) $2MoS_2$, (4×4) $2MoS_2$-2(H2-PPY)-FAR, and (4×4) $2MoS_2$-2(H2-PPY); (b) (4×4) $2MoS_2$-2(Mn(II)-PPY)-FAR and (4×4) $2MoS_2$-2(Mn(II)-PPY); (c) (4×4) $2MoS_2$-2(Mn(III)-PPY)-FAR and (4×4) $2MoS_2$-2(Mn(III)-PPY).

In order to understand the TDOS of the 1T' phase (4×4) $2MoS_2$-2(H2-PPY) or (4×4) $2MoS_2$-2(Mn-PPY), we considered two other systems in the 1T′ phase: (4×4) $2MoS_2$ and (4×4) $2MoS_2$-2(H2-PPY-FAR or Mn-PPY-FAR). $2MoS_2$ represents non-intercalated $2MoS_2$ with the optimized *c* parameter. $2MoS_2$-2(H2-PPY-FAR or Mn-PPY-FAR) denotes an intercalated complex with *c* greater than the equilibrium value by 2.00 Å, so that there is only weak interaction between the MoS_2 layers and PPY molecules. A comparison of the TDOS of three systems indicates that the TDOS around the Fermi level increases significantly by the intercalation in the FAR complexes, which can be ascribed to charge transfer. Subsequent reduction of *c* to the equilibrium value introduces (i) a broadening of the TDOS due to the interaction of the MoS_2 with the PPY and (ii) an upward shift of the Fermi level due to further charge transfer. The TDOS is more enhanced in the $2MoS_2$-2(Mn(II)-PPY) and $2MoS_2$-2(Mn(III)-PPY) than in the $2MoS_2$-2(H2-PPY).

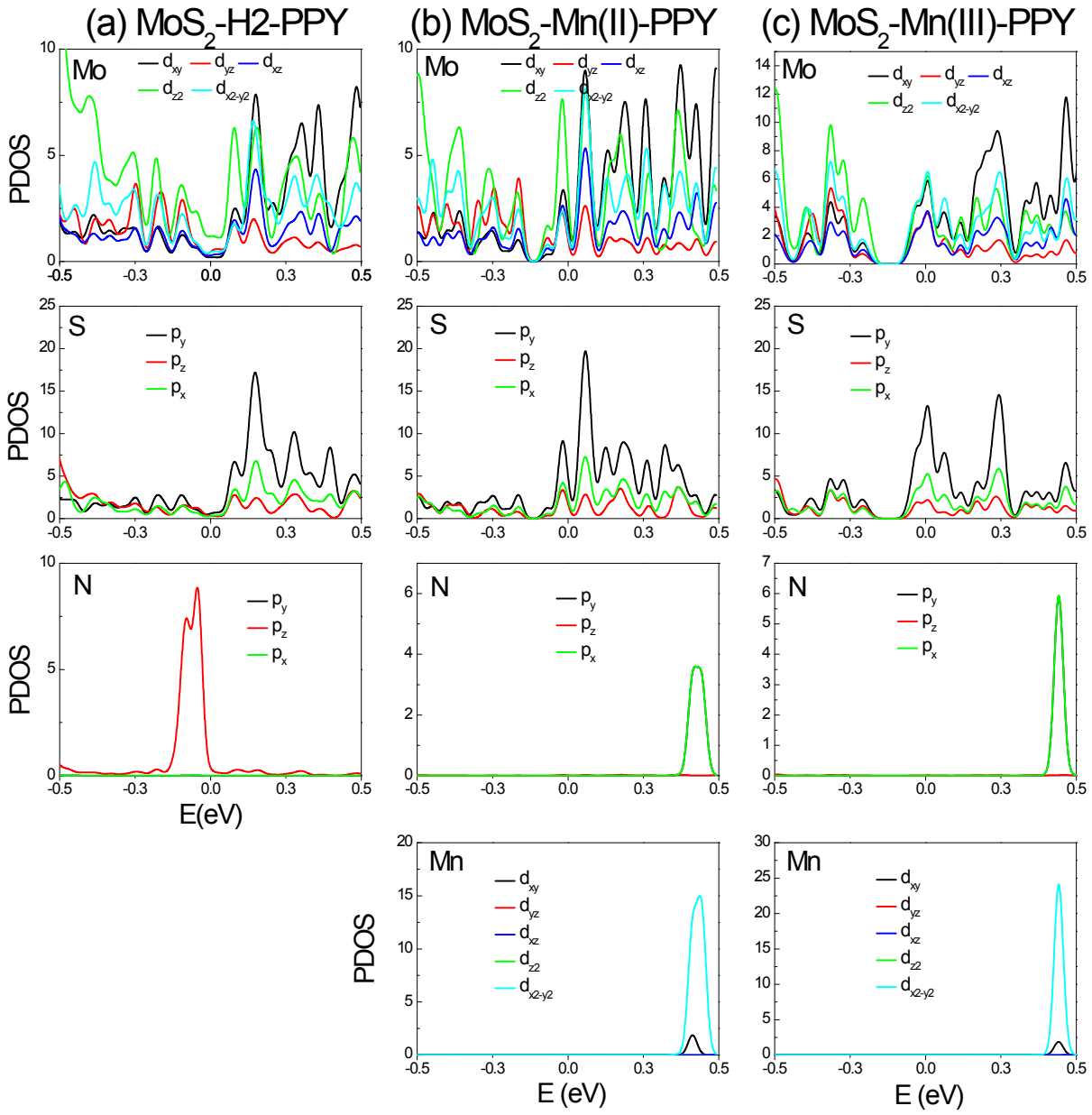

Figure S13. PDOS of (a) Mo, S, and N components for (4×4) $2MoS_2$-2(H2-PPY); Mo, S, N, and Mn components for (b) (4×4) $2MoS_2$-2(Mn(II)-PPY) and (c) (4×4) $2MoS_2$-2(Mn(III)-PPY).

In order to understand why TDOS is more enhanced in the $2MoS_2$-2(Mn-PPY) than the $2MoS_2$-2(H2-PPY), we compared the partial DOS (PDOS) of the constituents. The PDOS of Mn at E < 0.4 eV indicates negligible contribution to the TDOS. Remarkably, the PDOS of $2MoS_2$-2(Mn-PPY) shows significant increase of *d*(Mo) and *p*(S) states, particularly d_{xy}(Mo),

d_{x2-y2} (Mo), and the p_y(S) state that hybridizes with the *d* states just above the Fermi level. The d_{xy}(Mo) and d_{x2-y2} (Mo) states are more stabilized than those of the H2-PPY complex. This can be ascribed to the positive charge of proximal Mn-PPY being higher than that of H2-PPY, which is, in turn, due to better accommodation of electrons in the d_{z2} (Mo) state. As a result, the two *d*(Mo) states become more susceptible to extra electrons supplied by external bias. On the other hand, the d_{xz}(Mo) and d_{yz}(Mo) states still lie at the higher energies, because their symmetries are different from that of d_{z2} (Mo) state with respect to the *p*(S) orbitals at the top and bottom parts of the same layer.

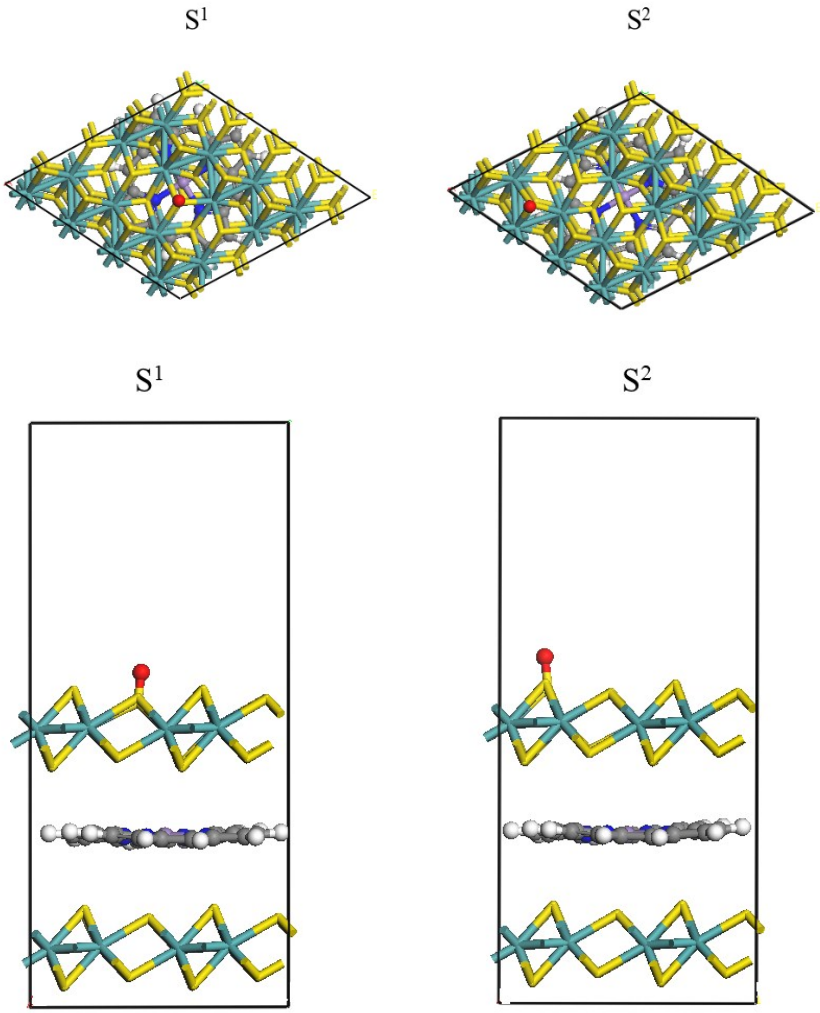

Figure S14. Structures of (4×4) $2MoS_2$-Mn(II)-PPY in slab geometry, showing the two different adsorption sites (S^1 and S^2) for an H^+ ion (red balls) for Volmer reaction. Turquoise, yellow, violet, grey, blue, and white balls of the complex represent the Mo, S, Mn, C, N, and H atoms, respectively. The top and side views are shown.

For computational efficiency, we adopted a supercell of (4×4) $2MoS_2$ with one PPY molecule. Again, the CINEB calculation was done with spin-polarization for the Mn-PPY complex. More accurate calculation should require antiferromagnetic coupling of spins in a supercell twice as large. The error in our simpler calculation can be roughly estimated from $\Delta E_{AFM\text{-}FM}$, the difference in total energy for the complex along the *c* axis with the antiferromagnetic and ferromagnetic couplings. The value of $\Delta E_{AFM\text{-}FM}$ (=16 meV) per PPY molecule is indeed small, supporting the accuracy of our calculation.

IV. References

S1. C. C. L. McCrory, S. Jung, I. M. Ferrer, S. M. Chatman, J. C. Peters and T. F. Jaramillo, *J. Am. Chem. Soc.*, 2015, **137**, 4347-4357.

S2. Y. Yin, J. Han, Y. Zhang, X. Zhang, P. Xu, Q. Yuan, L. Samad, X. Wang, Y. Wang, Z. Zhang, P. Zhang, X. Cao, B. Song and S. Jin, *J. Am. Chem. Soc.*, 2016, **138**, 7965-7972.

S3. (a) G. Kresse, and J. Hafner, *Phys. Rev. B*, 1993, **47**, 558. (b) G. Kresse and J. Furthmüller, *Phys. Rev. B*, 1996, **54**, 11169.

S4. G. Kresse and D. Joubert, *Phys. Rev. B*, 1999, **59**, 1758.

S5. S. Grimme, *J. Comput. Chem.*, 2006, **27**, 1787.

S6. A. I. Liechtenstein, V. I. Anisimov and J. Zaanen, *Phys. Rev. B*, 1995, **52**, R5467.

S7. G. Henkelman, B. P. Uberuaga and H. Jónsson, *J. Chem. Phys.*, *2000,* **113**, 9901.

S8. I. S. Kwon, I. H. Kwak, H. G. Abbas, G. Jung, Y. Lee, J. Park, S. J. Yoo, J. G. Kim and H. S. Kang, *Nanoscale*, 2018, **10**, 11349-11356.

S9. I. H. Kwak, I. S. Kwon, H. G. Abbas, G. Jung, Y. Lee, T. T. Debela, S. J. Yoo, J. G. Kim, J. Park and H. S. Kang, *Nanoscale*, 2018, **10**, 14726-14735.

S10. J. Xie, H. Zhang, S. Li, R. Wang, X. Sun, M. Zhou, J. Zhou, X. W. Lou and Y. Xie, *Adv. Mater.,* 2013*,* **25***,* 5807-5813.

S11. D. Voiry, M. Salehi, R. Silva, T. Fujita, M. Chen, T. Asefa, V. B. Shenoy, G. Eda and M. Chhowalla, *Nano Lett.,* 2013, **13**, 6222-6227.

S12. Z. Wu, C. Tang, P. Zhou, Z. Liu, Y. Xu, D. Wang and B. Fang, *J. Mater. Chem. A,* 2015, **3**, 13050-13056.

S13. D. Voiry, R. Fullon, J. Yang, C. C. C. Silva, R. Kappera, I. Bozkurt, D. Kaplan, M. J. Lagos, P. E. Batson, G. Gupta, A. D. Mohite, L. Dong, D. Er, V. B. Shenoy, T. Asefa and M. Chhowalla, *Nat. Mater.,* 2016*,* **15***,* 1003-1009.

S14. X. Geng, W. Sun, W. Wu, B. Chen, A. A. Hilo, M. Benamara, H. Zhu, F. Watanabe, J. Cui and T. Chen, *Nat. Commun.,* 2016, **7**, 10672.

S15. J. Zhang, J. Wu, H. Guo, W. Chen, J. Yuan, U. Martinez, G. Gupta, A. Mohite, P. M. Ajayan and J. Lou, *Adv. Mater.,* 2017*,* **29***,* 1701955.

S16. D. Wang, X. Zhang, S. Bao, Z. Zhang, H. Fei and Z. Wu, *J. Mater. Chem. A,* 2017, **5**, 2681-2688.

S17. E. E. Benson, H. Zhang, S. A. Schuman, S. U. Nanayakkara, N. D. Bronstein, S. Ferrere, J. L. Blackburn and E. M. Miller, *J. Am. Chem. Soc.,* 2018, **140***,* 441-450.

S18. C. Tan, Z. Luo, A. Chaturvedi, Y. Cai, Y. Du, Y. Gong, Y. Huang, Z. Lai, X. Zhang, L. Zheng, X. Qi, M. H. Goh, J. Wang, S. Han, X. J. Wu, L. Gu, C. Kloc and H. Zhang, *Adv. Mater*., 2018, **30***,* 1705509.

S19. L. Lin, N. Miao, Y. Wen, S. Zhang, P. Ghosez, Z. Sun and D. A. Allwood, *ACS Nano*, **2016**, *10*, 8929-8937.

S20. C. Tsai, H. Li, S. Park, J. Park, H. S. Han, J. K. Nørskov, X. Zheng and F. Abild-Pedersen, *Nat. Commun*., 2017, **8**, 15113.

S21. Y. Shi, Y. Zhou, D. R. Yang, W. X. Xu, C. Wang, F. B. Wang, J. J. Xu, X. H. Xia and H. Y. Chen, *J. Am. Chem. Soc.*, 2017, **139**, 15479−15485

S22. Z. Luo, Ouyang, Y.; Zhang, H.; Xiao, M.; Ge, J.; Jiang, Z.; J. Wang, D. Tang, X. Cao, C. Liu and W. Xing, *Nat. Commun*., 2018, **9**, 2120.

S23. K. Nakamoto, Infrared and Raman Spectra of Inorganic and Coordination Compounds.4th Ed. Jon & Wiley Sons (1986).

S24. M. Aydin, *Vibrational Spectroscopy*, 2013, **68**, 141-152.

S25. D.; Yang, S. J. Sandoval, W. M. R. Divigalpitiya, J. C. Irwin and R. F. Frindt, *Phys. Rev. B*, 1991, **43**, 12053-12056.